

Single nuclear spin detection and control in a van der Waals material

Xingyu Gao,^{1,*} Sumukh Vaidya,^{1,*} Kejun Li,^{2,3} Saakshi Dikshit,⁴ Shimin Zhang,³
Peng Ju,¹ Kunhong Shen,¹ Yuanbin Jin,¹ Yuan Ping,^{2,3} and Tongcang Li^{1,4,5,6,†}

¹*Department of Physics and Astronomy, Purdue University, West Lafayette, Indiana 47907, USA*

²*Department of Physics, University of California, Santa Cruz, CA, 95064, USA*

³*Department of Materials Science and Engineering, University of Wisconsin-Madison, 53706, USA*

⁴*Elmore Family School of Electrical and Computer Engineering,*

Purdue University, West Lafayette, Indiana 47907, USA

⁵*Purdue Quantum Science and Engineering Institute,*

Purdue University, West Lafayette, Indiana 47907, USA

⁶*Birck Nanotechnology Center, Purdue University, West Lafayette, Indiana 47907, USA*

(Dated: September 4, 2024)

Optically active spin defects in solids [1, 2] are leading candidates for quantum sensing [3, 4] and quantum networking [5, 6]. Recently, single spin defects were discovered in hexagonal boron nitride (hBN) [7–11], a layered van der Waals (vdW) material. Due to its two-dimensional structure, hBN allows spin defects to be positioned closer to target samples than in three-dimensional crystals, making it ideal for atomic-scale quantum sensing [12], including nuclear magnetic resonance (NMR) of single molecules. However, the chemical structures of these defects [7–11] remain unknown, and detecting a single nuclear spin with an hBN spin defect has been elusive. In this study, we created single spin defects in hBN using ¹³C ion implantation and identified three distinct defect types. We observed both $S = 1$ and $S = 1/2$ spin states within a single hBN spin defect, with only the $S = 1/2$ states showing strong hyperfine interactions with nearby ¹³C nuclear spins. For the first time, we demonstrated atomic-scale NMR and coherent control of individual nuclear spins in a vdW material. By comparing experimental results with density-functional theory calculations, we propose chemical structures for these spin defects. Our work advances the understanding of single spin defects in hBN and provides a pathway to enhance quantum sensing using hBN spin defects with nuclear spins as quantum memories.

Solid-state spin defects have become a leading platform for a wide range of quantum technologies, including multinode quantum networking [5, 6] and quantum-enhanced sensing [3, 4]. These advances are largely driven by the spin-photon quantum interfaces, which utilize optically addressable coherent spins. Despite the success of various spin-photon systems, each material platform has intrinsic limitations, creating trade-offs depending on the specific application [1, 2]. Moreover, spin defects that operate at room temperature are rare. Recently, optically active spin defects in hexagonal boron nitride (hBN), a van der Waals (vdW) material, has garnered vast attention [7–11, 13]. The layered structure of hBN facilitates integration with nanophotonic devices [14] and provides an ideal platform for quantum sensing at the atomic scale [12]. hBN spin defects have been used for sensing magnetic fields [15–17], temperature [15, 16], strain [18], and beyond [19]. However, electron spins in hBN suffer from short spin coherence times [20–22].

Nuclear spins typically exhibit long coherence times thanks to their weak coupling with the local environment, making them ideal candidates for quantum registers [23]. By employing nuclear spins as ancillary qubits, we can overcome the limitation of electron spin coherence

times and enhance the sensitivity of a spin-based quantum sensor [24, 25]. This approach requires the ability to initialize, control, and read out individual nuclear spins [26, 27]. In the context of hBN spin defects, previous experiments used negatively charged boron vacancy (V_B^-) defects to polarize and read out nitrogen nuclear spin ensembles [28–31]. However, these experiments were limited to ensemble-level operations due to the low quantum efficiency of V_B^- defects. Moreover, the relatively short relaxation time of V_B^- electron spins ($T_1 < 20 \mu\text{s}$ at room temperature) restricted the maximum operational time of nuclear spins. Recently discovered single spin defects in hBN [7–11] enabled the readout of individual electron spins in hBN. However, the chemical structures of these single spin defects remain unidentified, and the control of individual nuclear spins in hBN or other vdW materials is still elusive.

In this article, we report the first realization of single nuclear spin detection and control using a carbon-related defect in hBN. Our study reveals three major types of spin defects in ¹³C implanted hBN, with remarkably high optically detected magnetic resonance (ODMR) contrasts of up to 200%. Two of these defect types are strongly coupled to nearby ¹³C nuclear spins. We observe the coexistence of $S = 1$ and $S = 1/2$ states within a single spin defect, though only the $S = 1/2$ states exhibit strong coupling to ¹³C nuclear spins, with coupling strengths reaching up to 300 MHz. The strong hyperfine

* These authors contributed equally to this work.

† tcli@purdue.edu

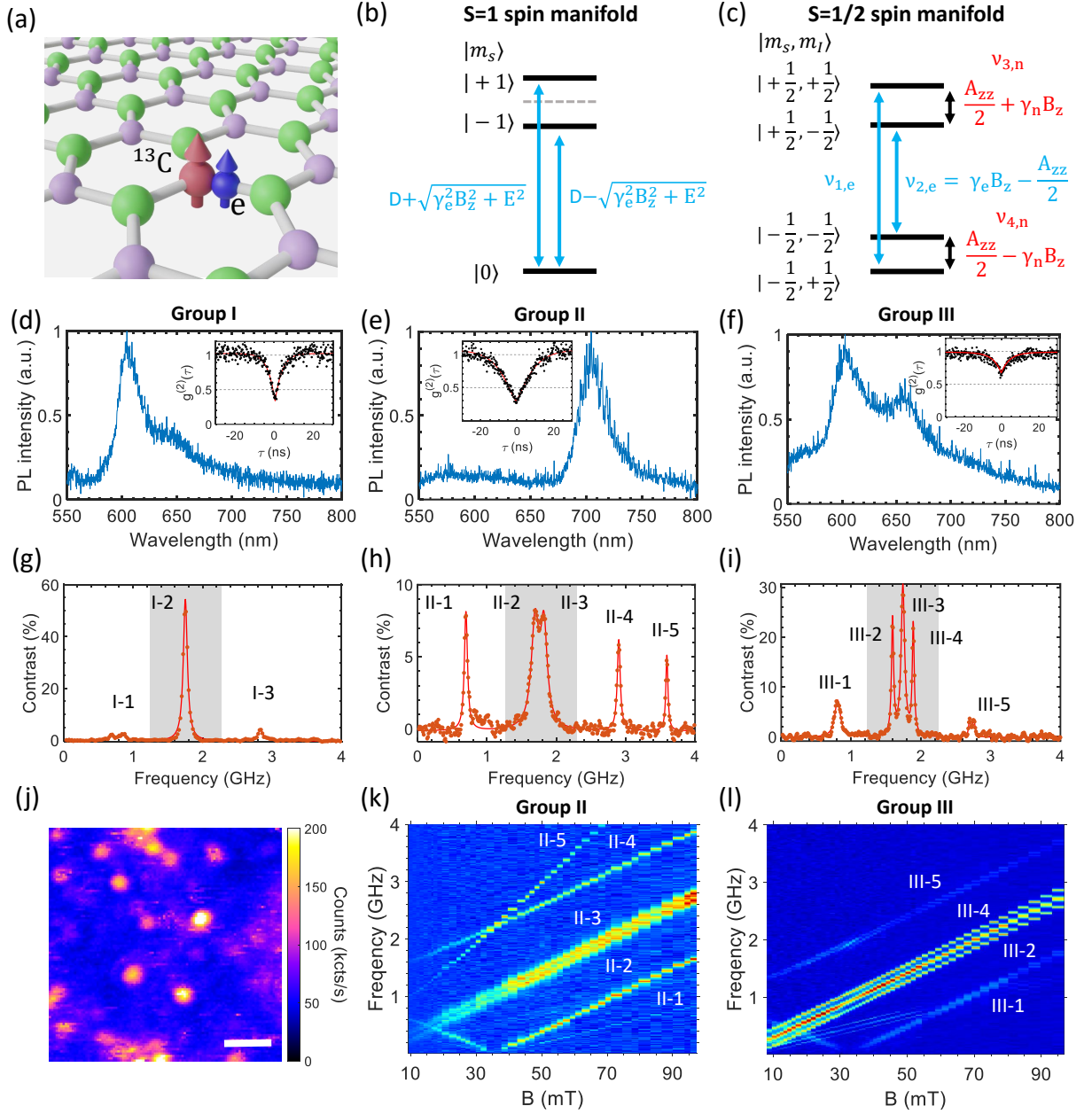


Figure 1. **Observation of three types of single spin defects in hBN** (a) An illustration of a carbon-related spin defect consisting of an electron spin and a ^{13}C nuclear spin. (b) An energy level diagram of a spin $S = 1$ ground state in an out-of-plane magnetic field B_z . (c) An energy level diagram of a spin $S = 1/2$ ground state, coupled to a ^{13}C nuclear spin ($I = 1/2$). A_{zz} is the hyperfine interaction strength. ν_1 and ν_2 are the two electron spin transitions. (d)-(f) Optical spectra of Defect 1-3, belonging to Group I-III, respectively. (g)-(i) ODMR spectra of Defect 1-3. An out-of-plane external magnetic field of 62.5 mT is applied. The numbers of peaks at the center (shaded area) are different for Group I-III defects. (j) A PL confocal map showing isolated bright emitters in hBN. Scale bar: $2 \mu\text{m}$. (k)-(l) Magnetic field dependent ODMR spectra of Defect 2 in Group II (k), and Defect 3 in Group III (l).

coupling results in well resolved hyperfine structures, enabling the initialize and readout of single nuclear spins assisted by a defect electron spin. We also demonstrate robust coherent control of a ^{13}C nuclear spin and perform Ramsey and Hahn Echo measurements of the nuclear spin. The dephasing and coherence times of a typ-

ical ^{13}C nuclear spin in hBN at room temperature are measured to be $T_2^* = 16.6 \mu\text{s}$ and $T_2 = 162 \mu\text{s}$, respectively. Our density-functional theory calculations suggest that $\text{C}_B^+ \text{C}_N^0$ donor-acceptor pairs (DAP) and $\text{C}_B \text{O}_N$ are likely candidates for the two types of spin defects with large hyperfine interactions.

Single spin defects in ^{13}C implanted hBN

We create carbon-related spin defects in hBN [8, 9, 11] (Fig. 1) by $^{13}\text{CO}_2$ (99% ^{13}C) ion implantation and thermal annealing. A confocal photoluminescence (PL) map reveals isolated emitters, as depicted in Fig. 1(j). Their optical spectra spread from 570 nm to 700 nm, depending on different defects (Figure 1(d)-(f)). Photon correlation measurements suggest that some defects are single photon emitters ($g^{(2)}(0) < 0.5$). To verify the spin properties, we perform ODMR measurements by turning the microwave on and off while collecting the emitted photons. The ODMR contrast C is determined by the ratio of photon count rates when the microwave is on (N_{on}) or off (N_{off}): $C = N_{\text{on}}/N_{\text{off}}$. In contrast to previous reports of $S = 1/2$ spin defects with only a single resonant peak in ODMR [7–10], we observe three distinct ODMR spectra with multiple resonances (Fig. 1(g)-(i)). These ODMR spectra feature a center branch (shaded areas in Fig. 1(g)-(i)) comprising multiple resonances that are assigned to hyperfine structures, along with additional side resonances located approximately 1 GHz away from the center branch. To understand the origination of the multiple resonances shown in the ODMR spectra, we first describe the system using the spin Hamiltonian

$$H = DS_z^2 + E(S_x^2 - S_y^2) + \gamma_e \mathbf{B} \cdot \mathbf{S} + \sum_i \mathbf{S} \cdot \mathbf{A}_i \cdot \mathbf{I}_i + \gamma_n \mathbf{B} \cdot \mathbf{I}_i, \quad (1)$$

where γ_e and γ_n are the electron spin and the nuclear spin gyromagnetic ratios, and \mathbf{B} is the external magnetic field. \mathbf{S} denotes the electronic spin operator with $S = 1$ or $1/2$. D and E together are the zero-field splitting (ZFS) parameters, which are non-zero for the $S = 1$ states (Figure 1(b)) but vanish for the $S = 1/2$ states (Figure 1(c)). \mathbf{I}_i denotes the nuclear spin operator for the i -th nuclear spin coupled to the defect electron. Specifically, $I = 1/2$ for ^{13}C nuclear spins, $I = 1$ for ^{14}N nuclear spins, and $I = 3/2$ for ^{11}B nuclear spins.

Based on ODMR spectra as shown in Fig. 1(g)-(i), we categorize the spin defects into three major groups, Group I-III, according to the number of peaks in the center branch. Individual peaks are labeled based on the defect group. The hyperfine splitting of Group II and III defects are determined to be 130 MHz and 300 MHz, respectively. It is worth noting that the 300 MHz hyperfine splitting is determined by the separation between the transitions III-2 and III-4. As will be discussed later, we assign the center peak III-3 to a second electron spin that weakly couples to the primary electron spin, suggested by the recently proposed spin pair model [32, 33]. The ODMR contrast can be as high as 200%. A good single hBN spin defect in our sample has a typical sensitivity of $5 \mu\text{T}/\sqrt{\text{Hz}}$ for DC magnetic field sensing, calculated by $(8\pi/3\sqrt{3}) \cdot (1/\gamma_e) \cdot (\Delta\nu/C\sqrt{T})$ [29], where $\Delta\nu$ is linewidth (20 MHz), C is the contrast (30 %) and I is the photon count rate (170 kcts/s).

To better understand the spin transitions, we measure

the ODMR spectra as functions of out-of-plane magnetic fields (Figure 1(k) and (i)). The results reveal an absence of zero field splitting (ZFSs) in the center branch, suggesting a $S = 1/2$ spin manifold. In contrast, the side resonances (II-1, II-4, III-1 and III-5) confirm non-zero ZFSs and disperse with a g -factor of 2. These resonances can be described by the $S = 1$ spin Hamiltonian of Eq. 1, with a finite D (typically ~ 1 GHz) and E along an out-of-plane quantization axis. This is distinct from the recent observation about a spin-triplet defect with an in-plane quantization axis [11], making it easier for magnetic field alignment. The additional peak II-5 of Defect 2 locates at the frequency $\nu_5 = \nu_1 \pm \nu_4$ and has an anti-level crossing with II-4 at 37 mT, implying a double quantum transition. The assignment of $S = 1$ and $S = 1/2$ spin manifolds for these transitions is further supported by the measured ratio of Rabi oscillation frequencies ($1.37 \approx \sqrt{2}$) when the microwave is applied at line II-1 ($S = 1$) and II-2 ($S = 1/2$).

Detection of single ^{13}C nuclear spins in hBN

The well-resolved hyperfine structures enable us to distinguish different defect groups through two-dimensional (2D) mapping of the ODMR contrast at specific microwave driving frequencies. Figure 2 (a)-(c) present the ODMR contrast distribution of a ^{13}C -implanted hBN with microwaves resonant at I-2, II-2 and III-2 transitions (Fig. 1(g)-(i)), respectively. All three maps reveal multiple spots with finite contrasts, enabling us to locate Group II and Group III defects. In contrast, no ODMR signal is observed in ^{12}C -implanted hBN when microwaves are applied at the II-2 and III-2 transitions.

Besides ODMR, optically detected nuclear magnetic resonance (ODNMR) (Figure 2(g)) of ^{13}C nuclear spins can provide further insights into the electron-nuclear hyperfine coupling. Here we conduct these measurements at the center branch of Group II and III defects. For both Defect 2 and Defect 3, we observe two closely spaced resonances in ODNMR at approximately half the frequencies of the hyperfine splitting observed in ODMR (Figure 2(h)-(i)). Such a feature verifies the $S = 1/2$ configuration of the defect electron spin for these transitions. For a $S = 1$ configuration, we expect the ODNMR resonance frequency to be the same as the hyperfine splitting in ODMR. The two-peak structure originates from the external magnetic field and/or a weaker hyperfine coupling to a second electronic spin. We also notice that different nuclear resonance frequencies are obtained when the microwave is applied at III-2 (III-4) and III-3. These features further verify two $S = 1/2$ electron spins are involved in Defect 3.

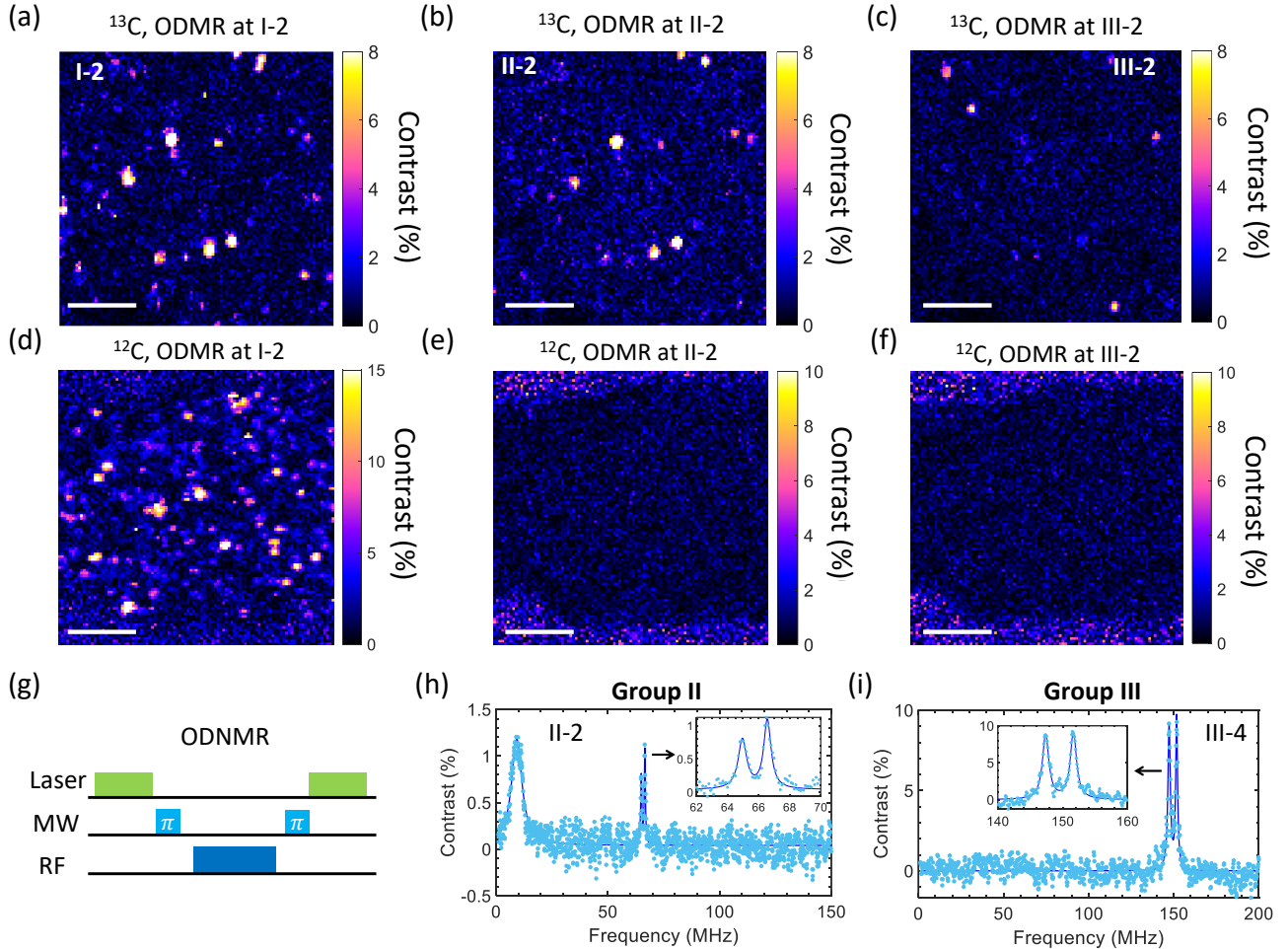


Figure 2. **Optical detection of ^{13}C nuclear spins in hBN** (a)-(c) ODMR contrast map of ^{13}C implanted hBN by driving a microwave at (a) 2.01 GHz, resonance I-2 of Group I defects; (b) 1.95 GHz, resonance II-2 of Group II defects; and (c) 1.86 GHz, resonance III-2 of Group III defects. (d)-(f) ODMR contrast map of ^{12}C implanted hBN by driving the microwave at (d) I-2, (e) II-2, and (f) III-2. The contrast fluctuation outside the hBN is caused by the low photon counts collected from the background. Scale bars are $5\ \mu\text{m}$. A 71.5 mT magnetic field is applied out-of-plane (perpendicular to the hBN nanosheet). (g) An illustration of the ODNMR sequence. (h) An ODNMR spectrum of Defect 2 by driving the microwave at II-2. (i) An ODNMR spectrum of Defect 3 by driving the microwave at III-4.

Coherent control of a ^{13}C nuclear spin in hBN

The well-isolated electron spin transitions at III-2 and III-4 (Fig. 1(i)) enable coherent manipulation of individual electron spin states associated with different nuclear spin states. This capability allows for the initialization, control, and readout of a nuclear spin via the electron spin, without the need for strong magnetic fields or level anticrossing (LAC) [28–31].

To polarize the ^{13}C nuclear spin, we first use a laser pulse to initialize the electron state (assuming $|m_s = -1/2\rangle$). Next, we apply a SWAP gate (Figure 3(a)) to swap the electron spin state and nuclear spin state, after which the nuclear spin is initialized to $|\uparrow\rangle$ (or $|\downarrow\rangle$). To estimate the fidelity of nuclear spin initialization, we measure the electron spin ODMR sig-

nal after the SWAP gate and calculate the polarization according to the imbalance between III-2 and III-4 (Figure 3(b)). We determine the nuclear spin polarization to be approximately 43% (-33%) using the equation $P = (\rho_4 - \rho_2)/(\rho_4 + \rho_2)$, where ρ_j represents the amplitude of resonance III-j. A higher nuclear spin polarization of 60% can be achieved with another defect.

For nuclear spin coherent control, we use the protocol depicted in Figure 3(c). After polarizing the nuclear spin, another 10- μs laser pulse re-initializes the electron spin state. Subsequently, we park the frequency of the selective RF pulse while varying its pulse duration τ . Finally, the nuclear spin state is read out via the spin defect using a selective microwave π pulse and a 5- μs laser pulse. Figure 3(d) shows the resulting nuclear spin Rabi oscillations. The oscillation persists for 40 μs without significant decay, yielding a π -gate fidelity of 99.75%. The

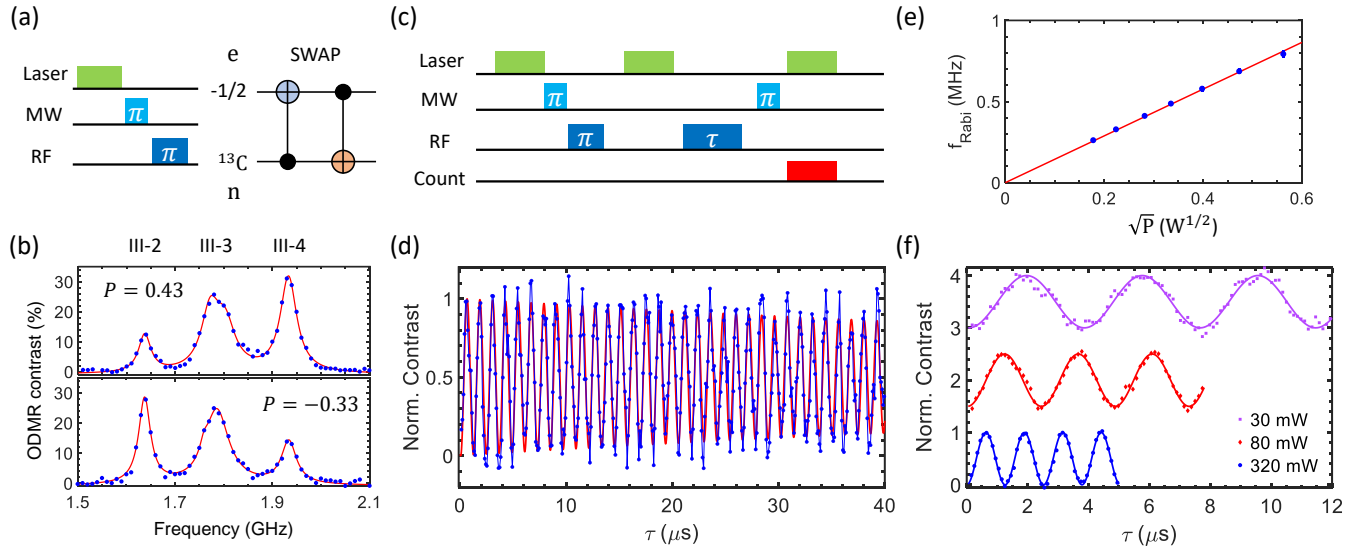


Figure 3. **Initialization and coherent control of a ^{13}C nuclear spin** (a) An illustration of the pulse sequence (left panel) for nuclear spin initialization. We use a SWAP gate (right panel) to transfer the electron spin polarization to the ^{13}C nuclear spin. (b) ODMR signal after nuclear spin initialization. One of the two peaks (III-2 and III-4) dominates, yielding a nuclear spin polarization of 0.43 (top panel) and -0.33 (bottom panel), depending on the direction of initialization. (c) Pulse sequence for nuclear spin coherent control. (d) An example of nuclear spin Rabi oscillation, persisting for 40 μs without significant decay. The blue curve is the experimental data, and the red curve is fitting. (e) Nuclear spin Rabi frequency as a function of the square root of the RF power. (f) Nuclear spin Rabi oscillations taken at different RF powers: 30 mW (purple squares), 80 mW (Red diamonds), and 320 mW (Blue dots).

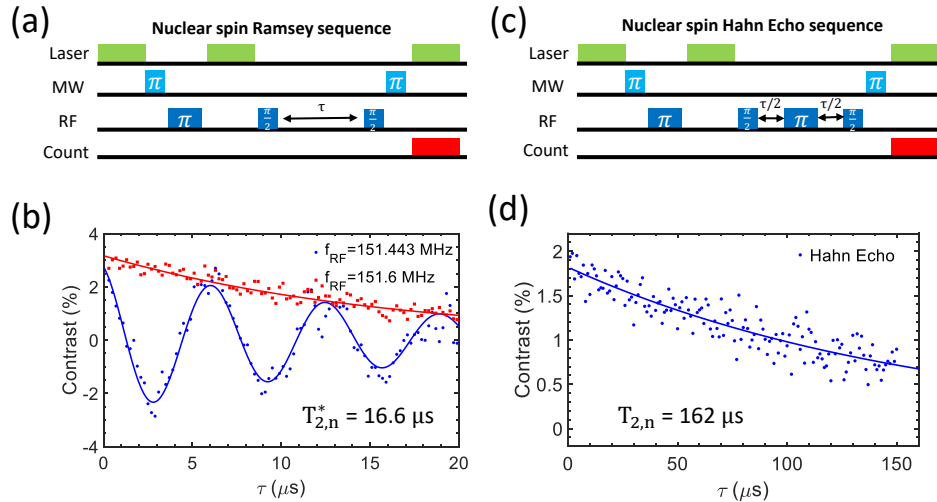


Figure 4. **Spin coherence of a ^{13}C nuclear spin** (a) The pulse sequence of nuclear spin Ramsey interferometry. (b) The nuclear spin Ramsey fringe. The measurements are performed when the RF frequency is in resonance with the nuclear spin transition (red squares) or slightly detuned from the resonance (blue dots). The fitting of the oscillation showing an inhomogeneous dephasing time of $T_{2,n}^* = 16.6 \mu\text{s}$. (c) The pulse sequence of nuclear spin Hahn Echo. (d) The nuclear spin Hahn Echo measurement shows a slow decay with $T_{2,n} = 162 \mu\text{s}$.

extended operational time for nuclear spins is attributed to the long electron spin relaxation time ($T_{1,e} = 144 \mu\text{s}$) of this carbon-related spin defect, which is an order of magnitude longer than that of V_B^- spin ensembles [28, 29]. By repeating the measurements at different RF powers, we observe a clear power dependence of the oscill-

lations (Figure 3(f)), where the nuclear Rabi frequency is linearly proportional to the amplitude of the RF field (Figure 3(g)).

We further characterize the nuclear spin coherence via Ramsey and Hahn Echo sequences, as illustrated in Figure 4 (a)-(b). In the Ramsey interferometry, when RF

pulses are applied exactly in resonance with the nuclear spin transitions, we observe a slow decay in 20 μs . With a slight detuning of the RF frequency, an additional oscillation is observed alongside the original decay. By fitting the oscillation using the equation $a \cdot \cos(\omega\tau + \phi)e^{-\tau/T_{2,n}^*} + c$, we determine the inhomogeneous dephasing time to be $T_{2,n}^* = 16.6 \mu\text{s}$ and the oscillation frequency to be the same as the detuning. Figure 4(d) shows the exponential decay measured by the nuclear spin Hahn Echo sequence, revealing a nuclear spin coherence time of $T_{2,n} = 162 \mu\text{s}$. The nuclear spin coherence time is comparable with the electron spin relaxation time $T_{1,e} = 144 \mu\text{s}$, suggesting the measurement is limited by the electronic spin lifetime.

Identifying chemical structures

To identify possible chemical structures of the observed single spin defects, we perform first-principles calculations for the static properties and hyperfine interaction tensors. These properties can be directly compared with experimental results. Recent studies suggested the metastable configuration of the $S = 1/2$ spin manifolds, while the optical transitions are supposed to come from the singlet state ($S = 0$) [32, 33]. Therefore, for the simulation of ODMR using hyperfine tensors, we mainly focus on the $S = 1/2$ spin manifolds. And we compare the optical spectra to the calculated ZPLs in the singlet manifolds.

Among the calculated candidates, $C_B C_N$ -DAP-L [34] is a likely candidate for Group II defects (Figure 5(a)). This defect has a $C_B C_N$ dimer structure with a larger separation (L lattice distance) between the two point defects. The positively charged state ($C_B^+ C_N^0$ -DAP-L) contains an $S = 1/2$ manifold, with a predicted hyperfine coupling strength of 135 MHz for the $^{13}\text{C}_N$ nuclear spin, closely matching the observed hyperfine coupling of 130 MHz. The simulated ODMR spectrum also aligns well with the measured ODMR, as shown in Figure 5(b). Since the spin density is primarily localized at the C_N site and is barely affected by the distance L , the hyperfine coupling strength remains nearly unchanged for different L values. In contrast, the zero-photon line (ZPL) of $C_B^0 C_N^0$ -DAP-L ($S = 0$) is strongly affected by the distance L . For example, the ZPL ranges from 1.75 eV to 2.14 eV as L varies from $\sqrt{7}$ to 4, agreeing well with our observed peak wavelength ranging from 585 nm (2.12 eV) to 700 nm (1.77 eV).

The $C_B O_N$ defect can be the spin defect in the Group III defects that contributes to the large hyperfine splitting. The positively charged state ($q = 1$) has a spin doublet manifold ($S = 1/2$) (Fig. 5(c)) with a hyperfine interaction strength of $A_{zz} = 314$ MHz, which is close to the measured hyperfine coupling of 300 MHz. In Fig. 5(d), the simulated ODMR linewidth induced by the nuclear spin bath is 23 MHz, which is also close to the measured linewidth (16 MHz) under a weak microwave

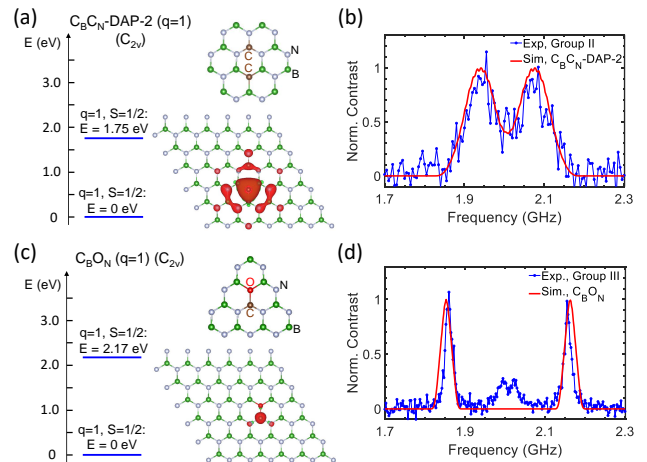


Figure 5. **Spin defect candidates** (a) Chemical structure, spin density and energy-level diagram of the positively charged $C_B^+ C_N^0$ -DAP-2 defect. (b) Simulated ODMR spectrum of the positively charged $C_B^+ C_N^0$ -DAP-2 defect based on the calculated hyperfine coupling parameters. The simulation result (red curve) is compared with the experimental result (blue curve). (c) Chemical structure, electronic wavefunction and energy level diagram of the positively charged $C_B O_N$ defect. (d) Simulated ODMR spectrum of the positively charged $C_B O_N$ defect based on the calculated hyperfine coupling parameters. The simulation result (red curve) is compared with the experimental result (blue curve).

drive. The center peak (III-3) in Fig. 5(d) is attributed to a nearby second spin defect.

Conclusion

In conclusion, we report the detection and coherent control of single ^{13}C nuclear spins using single hBN spin defects at room temperature. We find three distinct defect groups in $^{13}\text{CO}_2$ implanted hBN samples, categorized based on their ODMR spectra. We observe both $S = 1/2$ and $S = 1$ spin states within a single hBN spin defect, which displays quantum coherence at room temperature and ODMR contrast up to 200%. In addition, the electronic spin state can be readout using a reasonably long laser pulse of around 5 μs , yielding approximately one photon per readout pulse and a single-short spin readout fidelity of $\eta = 0.12$ (see Methods).

Leveraging the control of individual resonances within the well-resolved hyperfine structures, we demonstrate initialization, coherent control and readout of a single ^{13}C nuclear spin using spin defects in Group II and Group III. The nuclear spins exhibits coherence times that are orders of magnitudes longer than those of electronic spins in hBN, offering the potential for long-lived quantum registers. The well-resolved hyperfine structure, combined with the high readout efficiency of spin states enabled by the high ODMR contrasts and the extended nuclear spin coherence times, makes this approach promising for

achieving single-shot readout of individual nuclear spins [26]. This capability is crucial for implementing quantum error correction protocols in a quantum register [27]. Moreover, the ^{13}C nuclear spin can serve as a quantum memory to enhance quantum sensing with single hBN spin defects.

Methods

Sample preparation

The hBN thin flakes were tape-exfoliated from a monocrystalline hBN crystal and transferred onto Si/SiO₂ substrates. Then we irradiated the hBN flakes with 2.5 keV $^{13}\text{CO}_2$ (99.0% ^{13}C , Sigma-Aldrich) ions using a home-built ion implanter. The sample is then annealed at high temperature at 10^{-5} torr for 2 hours to activate the carbon-related defects. For ODMR measurements, we transferred the hBN flakes to a coplanar waveguide using the standard dry transfer method with propylene carbonate stamps. The waveguide is made of 200 nm thick silver with a 4 nm thick Al₂O₃ layer on top.

Estimation of nuclear spin polarization

We estimate the polarization of the ^{13}C nuclear spin by evaluating the imbalance between III-2 and III-4 in the ODMR spectrum. The ODMR is taken after the SWAP gate to transfer the electron polarization to the ^{13}C nuclear spin. By using the fitted relative populations of the hyperfine basis states, the polarization can be calculated by the equation

$$P = \frac{\sum_{m_I} m_I \rho_{m_I}}{I \sum_{m_I} \rho_{m_I}} = \frac{\rho_{1/2} - \rho_{-1/2}}{\rho_{1/2} + \rho_{-1/2}} \quad (2)$$

Spin readout fidelity

The fidelity of a single-shot spin readout is an important factor to estimate how efficiently one can determine the electronic spin state of a spin defect, which is highly dependent on the defect properties. The fidelity is defined by the signal-to-noise ratio from a single readout pulse and can be expressed as [35]

$$\eta_s = 1/\sigma_s = \left(1 + 2 \frac{\alpha_0 + \alpha_1}{(\alpha_0 - \alpha_1)^2}\right)^{-1/2}. \quad (3)$$

where α_0 and α_1 are the mean numbers of detected photons for a single measurement of the brighter state and

darker state, respectively. We estimate the fidelity based on the pulsed ODMR measurements. The pulsed ODMR contrast is 18% when we set readout duration at 5 μs under a $P_{MW}=60$ mW microwave drive. The contrast reaches 30% when $P_{MW}=2$ W. For each readout laser pulse, we obtain approximately 1 photon from the darker state under the 15 μW laser pumping. These yield the fidelity of 0.08 and 0.12 for $P_{MW}=60$ mW and $P_{MW}=2$ W, respectively.

Density-functional theory calculations

We use Quantum Espresso (QE) [36], an open-source plane-wave software, to perform the density-function theory (DFT) calculation. Both the Perdew-Burke-Ernzerhof (PBE) functional and the Heyd-Scuseria-Ernzerhof (HSE) hybrid functional (the factor of 0.32 for Fock exchange) [37, 38] are employed for the exchange-correlation interaction. We use Optimized Norm-Conserving Vanderbilt (ONCV) pseudopotential [39, 40] for the calculations of excitation energy, and the GIPAW pseudopotential [41] for the calculation of hyperfine interaction parameters and zero-field splitting (ZFS). We set the kinetic energy cutoff to be 55 Ry, which is adequate for converging the relevant properties. Geometry optimizations are carried out with a force threshold of 0.001 Ry/Bohr. We select the $6 \times 6 \times 1$ or higher supercell size of hBN for the calculations of hyperfine parameter and excitation energies. For these calculations, we sample a k-point mesh of $3 \times 3 \times 1$ for the calculation of excitation energies [42], and Γ point for the hyperfine parameters and ZFS [28, 42]. We calculate the zero-phonon line (ZPL) by the constraint occupation DFT (CDFT) method [43], the hyperfine parameters using the QE-GIPAW code [44], the ZFS by using the ZFS code [42], and we cross compare results between ZFS code and the PyZFS code [45].

Simulation of ODMR spectrum

The continuous wave (cw) ODMR spectra are simulated using the MATLAB toolbox EASYSPIN [46] based on data from the *Ab initio* calculations. EASYSPIN also takes the nuclear Zeeman and quadrupole interaction into account. Therefore, the cw ODMR linewidth can be determined according to the hyperfine couplings with the most abundant nuclear-spin-active isotopes: ^{13}C , ^{11}B and ^{14}N . In our simulation, we consider a ^{13}C nuclear spin, ten nearest ^{11}B nuclear spins and two proximate ^{14}N nuclear spins. The other nuclei, located further away, couple more weakly to the electron, scaling with $\propto 1/r^3$ (where r is the distance from the central carbon site), and thereby have a negligible effect on the ODMR linewidth.

-
- [1] Mete Atatüre, Dirk Englund, Nick Vamivakas, Sang-Yun Lee, and Joerg Wrachtrup. Material platforms for spin-based photonic quantum technologies. *Nature Reviews Materials*, 3(5):38–51, 2018.
- [2] Gary Wolfowicz, F Joseph Heremans, Christopher P Anderson, Shun Kanai, Hosung Seo, Adam Gali, Giulia

Galli, and David D Awschalom. Quantum guidelines for solid-state spin defects. *Nature Reviews Materials*, 6:906–925, 2021.

- [3] Christian L Degen, Friedemann Reinhard, and Paola Cappellaro. Quantum sensing. *Reviews of modern physics*, 89:035002, 2017.

- [4] Jiangfeng Du, Fazhan Shi, Xi Kong, Fedor Jelezko, and Jörg Wrachtrup. Single-molecule scale magnetic resonance spectroscopy using quantum diamond sensors. *Reviews of Modern Physics*, 96:025001, 2024.
- [5] Matteo Pompili, Sophie LN Hermans, Simon Baier, Hans KC Beukers, Peter C Humphreys, Raymond N Schouten, Raymond FL Vermeulen, Marijn J Tiggelman, Laura dos Santos Martins, Bas Dirkse, et al. Realization of a multinode quantum network of remote solid-state qubits. *Science*, 372:259–264, 2021.
- [6] CM Knaut, A Suleymanzade, Y-C Wei, DR Assumpcao, P-J Stas, YQ Huan, B Machielse, EN Knall, M Sutula, G Baranes, et al. Entanglement of nanophotonic quantum memory nodes in a telecom network. *Nature*, 629:573–578, 2024.
- [7] Nathan Chejanovsky, Amlan Mukherjee, Jianpei Geng, Yu-Chen Chen, Youngwook Kim, Andrej Denisenko, Amit Finkler, Takashi Taniguchi, Kenji Watanabe, Durga Bhaktavatsala Rao Dasari, et al. Single-spin resonance in a van der Waals embedded paramagnetic defect. *Nature materials*, 20:1079–1084, 2021.
- [8] Noah Mendelson, Dipankar Chugh, Jeffrey R Reimers, Tin S Cheng, Andreas Gottscholl, Hu Long, Christopher J Mellor, Alex Zettl, Vladimir Dyakonov, Peter H Beton, et al. Identifying carbon as the source of visible single-photon emission from hexagonal boron nitride. *Nature materials*, 20:321–328, 2021.
- [9] Hannah L Stern, Qiushi Gu, John Jarman, Simone Eizagirre Barker, Noah Mendelson, Dipankar Chugh, Sam Schott, Hoe H Tan, Henning Sirringhaus, Igor Aharonovich, et al. Room-temperature optically detected magnetic resonance of single defects in hexagonal boron nitride. *Nature communications*, 13(1):618, 2022.
- [10] Nai-Jie Guo, Song Li, Wei Liu, Yuan-Ze Yang, Xiaodong Zeng, Shang Yu, Yu Meng, Zhi-Peng Li, Zhao-An Wang, Lin-Ke Xie, et al. Coherent control of an ultrabright single spin in hexagonal boron nitride at room temperature. *Nature Communications*, 14(1):2893, 2023.
- [11] Hannah L Stern, Carmem M. Gilardoni, Qiushi Gu, Simone Eizagirre Barker, Oliver FJ Powell, Xiaoxi Deng, Stephanie A Fraser, Louis Follet, Chi Li, Andrew J Ramsay, et al. A quantum coherent spin in hexagonal boron nitride at ambient conditions. *Nature Materials*, pages 1–7, 2024.
- [12] Lingnan Shen, Di Xiao, and Ting Cao. Proximity-induced exchange interaction: A new pathway for quantum sensing using spin centers in hexagonal boron nitride. *The Journal of Physical Chemistry Letters*, 15(16):4359–4366, 2024.
- [13] Andreas Gottscholl, Mehran Kianinia, Victor Soltamov, Sergei Orlinskii, Georgy Mamin, Carlo Bradac, Christian Kasper, Klaus Krambrock, Andreas Sperlich, Milos Toth, et al. Initialization and read-out of intrinsic spin defects in a van der Waals crystal at room temperature. *Nature materials*, 19:540–545, 2020.
- [14] Joshua D Caldwell, Igor Aharonovich, Guillaume Cassabois, James H Edgar, Bernard Gil, and DN Basov. Photonics with hexagonal boron nitride. *Nature Reviews Materials*, 4:552–567, 2019.
- [15] Andreas Gottscholl, Matthias Diez, Victor Soltamov, Christian Kasper, Dominik Krauß, Andreas Sperlich, Mehran Kianinia, Carlo Bradac, Igor Aharonovich, and Vladimir Dyakonov. Spin defects in hBN as promising temperature, pressure and magnetic field quantum sensors. *Nature communications*, 12:4480, 2021.
- [16] AJ Healey, SC Scholten, T Yang, JA Scott, GJ Abrahams, IO Robertson, XF Hou, YF Guo, S Rahman, Y Lu, et al. Quantum microscopy with van der Waals heterostructures. *Nature Physics*, 19:87–91, 2023.
- [17] Mengqi Huang, Jingcheng Zhou, Di Chen, Hanyi Lu, Nathan J McLaughlin, Senlei Li, Mohammed Alghamdi, Dziga Djugba, Jing Shi, Hailong Wang, et al. Wide field imaging of van der Waals ferromagnet Fe_3GeTe_2 by spin defects in hexagonal boron nitride. *Nature communications*, 13:5369, 2022.
- [18] Xiaodan Lyu, Qinghai Tan, Lishu Wu, Chusheng Zhang, Zhaowei Zhang, Zhao Mu, Jesús Zúñiga-Pérez, Hongbing Cai, and Weibo Gao. Strain quantum sensing with spin defects in hexagonal boron nitride. *Nano Letters*, 22:6553–6559, 2022.
- [19] Sumukh Vaidya, Xingyu Gao, Saakshi Dikshit, Igor Aharonovich, and Tongcang Li. Quantum sensing and imaging with spin defects in hexagonal boron nitride. *Advances in Physics: X*, 8:2206049, 2023.
- [20] Andreas Gottscholl, Matthias Diez, Victor Soltamov, Christian Kasper, Andreas Sperlich, Mehran Kianinia, Carlo Bradac, Igor Aharonovich, and Vladimir Dyakonov. Room temperature coherent control of spin defects in hexagonal boron nitride. *Science Advances*, 7:eabf3630, 2021.
- [21] Ruotian Gong, Guanghui He, Xingyu Gao, Peng Ju, Zhongyuan Liu, Bingtian Ye, Erik A Henriksen, Tongcang Li, and Chong Zu. Coherent dynamics of strongly interacting electronic spin defects in hexagonal boron nitride. *Nature Communications*, 14(1):3299, 2023.
- [22] Roberto Rizzato, Martin Schalk, Stephan Mohr, Jens C Hermann, Joachim P Leibold, Fleming Bruckmaier, Giovanna Salvitti, Chenjiang Qian, Peirui Ji, Georgy V Astakhov, et al. Extending the coherence of spin defects in hBN enables advanced qubit control and quantum sensing. *Nature Communications*, 14(1):5089, 2023.
- [23] MV Gurudev Dutt, L Childress, L Jiang, E Togan, J Maze, F Jelezko, AS Zibrov, PR Hemmer, and MD Lukin. Quantum register based on individual electronic and nuclear spin qubits in diamond. *Science*, 316:1312–1316, 2007.
- [24] Sebastian Zaiser, Torsten Rendler, Ingmar Jakobi, Thomas Wolf, Sang-Yun Lee, Samuel Wagner, Ville Bergholm, Thomas Schulte-Herbrüggen, Philipp Neumann, and Jörg Wrachtrup. Enhancing quantum sensing sensitivity by a quantum memory. *Nature communications*, 7(1):12279, 2016.
- [25] Nabeel Aslam, Matthias Pfender, Philipp Neumann, Rolf Reuter, Andrea Zappe, Felipe Fávoro de Oliveira, Andrej Denisenko, Hitoshi Sumiya, Shinobu Onoda, Junichi Isoya, et al. Nanoscale nuclear magnetic resonance with chemical resolution. *Science*, 357(6346):67–71, 2017.
- [26] Philipp Neumann, Johannes Beck, Matthias Steiner, Florian Rempp, Helmut Fedder, Philip R Hemmer, Jörg Wrachtrup, and Fedor Jelezko. Single-shot readout of a single nuclear spin. *Science*, 329:542–544, 2010.
- [27] Gerald Waldherr, Yiqing Wang, S Zaiser, M Jamali, T Schulte-Herbrüggen, H Abe, T Ohshima, J Isoya, JF Du, P Neumann, et al. Quantum error correction in a solid-state hybrid spin register. *Nature*, 506:204–207, 2014.
- [28] Xingyu Gao, Sumukh Vaidya, Kejun Li, Peng Ju, Boyang Jiang, Zhuqing Xu, Andres E Llacsahuanga Allcca, Kun-

- hong Shen, Takashi Taniguchi, Kenji Watanabe, et al. Nuclear spin polarization and control in hexagonal boron nitride. *Nature Materials*, 21:1024–1028, 2022.
- [29] Ruotian Gong, Xinyi Du, Eli Janzen, Vincent Liu, Zhongyuan Liu, Guanghui He, Bingtian Ye, Tongcang Li, Norman Y Yao, James H Edgar, et al. Isotope engineering for spin defects in van der waals materials. *Nature Communications*, 15:104, 2024.
- [30] T Clua-Provost, A Durand, Z Mu, T Rastoin, J Fraunié, E Janzen, H Schutte, JH Edgar, G Seine, A Claverie, et al. Isotopic control of the boron-vacancy spin defect in hexagonal boron nitride. *Physical Review Letters*, 131:126901, 2023.
- [31] Shihao Ru, Zhengzhi Jiang, Haidong Liang, Jonathan Kenny, Hongbing Cai, Xiaodan Lyu, Robert Cernansky, Feifei Zhou, Yuzhe Yang, Kenji Watanabe, et al. Robust nuclear spin polarization via ground-state level anti-crossing of boron vacancy defects in hexagonal boron nitride. *Physical Review Letters*, 132:266801, 2024.
- [32] Islay O Robertson, Benjamin Whitefield, Sam C Scholten, Priya Singh, Alexander J Healey, Philipp Reineck, Mehran Kianinia, David A Broadway, Igor Aharonovich, and Jean-Philippe Tetienne. A universal mechanism for optically addressable solid-state spin pairs. *arXiv preprint arXiv:2407.13148*, 2024.
- [33] Raj N Patel, Rebecca EK Fishman, Tzu-Yung Huang, Jordan A Gusdorff, David A Fehr, David A Hopper, S Alex Breitweiser, Benjamin Porat, Michael E Flatté, and Lee C Bassett. Room temperature dynamics of an optically addressable single spin in hexagonal boron nitride. *Nano Letters*, 2024.
- [34] Philipp Auburger and Adam Gali. Towards ab initio identification of paramagnetic substitutional carbon defects in hexagonal boron nitride acting as quantum bits. *Physical Review B*, 104:075410, 2021.
- [35] David A Hopper, Henry J Shulevitz, and Lee C Bassett. Spin readout techniques of the nitrogen-vacancy center in diamond. *Micromachines*, 9:437, 2018.
- [36] Paolo Giannozzi, Stefano Baroni, Nicola Bonini, Matteo Calandra, Roberto Car, Carlo Cavazzoni, Davide Ceresoli, Guido L Chiarotti, Matteo Cococcioni, Ismaila Dabo, Andrea Dal Corso, Stefano de Gironcoli, Stefano Fabris, Guido Fratesi, Ralph Gebauer, Uwe Gerstmann, Christos Gougoussis, Anton Kokalj, Michele Lazzeri, Layla Martin-Samos, Nicola Marzari, Francesco Mauri, Riccardo Mazzarello, Stefano Paolini, Alfredo Pasquarello, Lorenzo Paulatto, Carlo Sbraccia, Sandro Scandolo, Gabriele Sclauzero, Ari P Seitsonen, Alexander Smogunov, Paolo Umari, and Renata M Wentzcovitch. QUANTUM ESPRESSO: A Modular and Open-Source Software Project for Quantum Simulations of Materials. *J. Phys.: Condens. Matter*, 21:395502, sep 2009.
- [37] Jochen Heyd, Gustavo E Scuseria, and Matthias Ernzerhof. Hybrid Functionals Based on a Screened Coulomb Potential. *J. Chem. Phys.*, 118:8207–8215, 2003. doi:10.1063/1.1564060.
- [38] Jochen Heyd, Gustavo E. Scuseria, and Matthias Ernzerhof. Erratum: “Hybrid functionals based on a screened Coulomb potential” [J. Chem. Phys. 118, 8207 (2003)]. *The Journal of Chemical Physics*, 124:219906, 06 2006. ISSN 0021-9606. doi:10.1063/1.2204597.
- [39] D. R. Hamann. Optimized Norm-Conserving Vanderbilt Pseudopotentials. *Phys. Rev. B*, 88(8):085117, aug 2013.
- [40] Martin Schlipf and François Gygi. Optimization Algorithm for the Generation of ONCV Pseudopotentials. *Comput. Phys. Commun.*, 196:36–44, 2015.
- [41] Christian Tantardini, Alexander G Kvasninin, and Davide Ceresoli. Gpaw pseudopotentials of d elements for solid-state nmr. *Mater.*, 15(9):3347, 2022.
- [42] Tyler J Smart, Kejun Li, Junqing Xu, and Yuan Ping. Intersystem Crossing and Exciton–Defect Coupling of Spin Defects in Hexagonal Boron Nitride. *npj Comput. Mater.*, 7:1–8, 2021. doi:10.1038/s41524-021-00525-5.
- [43] M Mackoitis-Sinkevičienė, Marek Maciaszek, Chris G Van de Walle, and Audrius Alkauskas. Carbon Dimer Defect as a Source of the 4.1 eV Luminescence in Hexagonal Boron Nitride. *Appl. Phys. Lett.*, 115(21):212101, 2019.
- [44] Nicola Varini, Davide Ceresoli, Layla Martin-Samos, Ivan Girotto, and Carlo Cavazzoni. Enhancement of dft-calculations at petascale: nuclear magnetic resonance, hybrid density functional theory and car–parrinello calculations. *Comput. Phys. Commun.*, 184:1827–1833, 2013.
- [45] He Ma, Marco Govoni, and Giulia Galli. PyZFS: A Python Package for First-Principles Calculations of Zero-Field Splitting Tensors. *J. Open Source Softw.*, 5:2160, 2020. doi:10.21105/joss.02160.
- [46] Stefan Stoll and Arthur Schweiger. Easyspin, a comprehensive software package for spectral simulation and analysis in epr. *Journal of magnetic resonance*, 178:42–55, 2006.